Available online at www.sciencedirect.com
ScienceDirect
Acta Materialia 57 (2009) 4081–4089
Acta MATERIALIA
www.elsevier.com/locate/actamat

Erbium and ytterbium solubilities and diffusivities in aluminum as determined by nanoscale characterization of precipitates

Marsha E. van Dalen [a,*], Richard A. Karnesky [a,1], Joseph R. Cabotaje [a], David C. Dunand [a], David N. Seidman [a,b]

[a] Department of Materials Science and Engineering, Northwestern University, 2220 Campus Dr., Evanston, IL 60208-3108, USA
[b] Northwestern University Center for Atom-Probe Tomography (NUCAPT), Northwestern University, 2220 Campus Dr., Evanston, IL 60208-3108, USA

Received 27 January 2009; received in revised form 1 May 2009; accepted 3 May 2009
Available online 6 June 2009

Abstract

Binary aluminum alloys with 0.03–0.06 at.% RE (RE = Yb or Er) were aged to produce coherent, nanosize Al_3RE precipitates in an α-Al matrix. The temporal evolution of precipitate radii and matrix concentrations at 300 °C were measured by transmission electron microscopy and local-electrode atom-probe tomography, respectively. The temporal dependence of the matrix concentration of each RE was utilized to determine its solubility in Al. The solubility and the coarsening rate constants were used to determine the diffusivity of each RE in α-Al and the α-Al/Al_3RE interfacial free energies at 300 °C. When compared to Sc, both Yb and Er exhibited smaller solubilities but larger diffusivities in α-Al and larger α-Al/Al_3RE interfacial energies.

Keywords: Aluminum alloys; Rare-earth elements; Diffusion; Precipitation; Coarsening

1. Introduction

Similar to Sc, the four heaviest rare-earth elements (RE = Er, Tm, Yb and Lu) exhibit an Al–Al_3RE eutectic reaction, with Al_3RE exhibiting a stable $L1_2$ crystal structure [1–5]. Unlike Sc, however, those REs have sparingly small solubilities in Al, even at the eutectic temperatures [3,6–8]. Even so, they are important ternary additions to Al–Sc alloys because they have the ability to substitute partially or fully for the more expensive Sc in the $Al_3(Sc_{1-x}RE_x)$ phase [2,3]. Also, these RE elements increase the lattice parameter of the intermetallic phase, thus increasing their unconstrained lattice parameter mismatches with α-Al, e.g. from 1.32% for pure Al_3Sc to 4.1% for pure and stoichiometric Al_3Er [2–5,9]. This increased lattice parameter mismatch improves the creep resistance of Al–Sc alloys by impeding dislocation climb over precipitates [10–12]. Furthermore, several researchers have observed yield strength increases at ambient temperature in Al alloys due to additions of Er [1,13–18] or Yb [19–21].

Three-dimensional local-electrode atom-probe tomography (APT) is a powerful instrument for measuring the solubility in dilute alloys since it can directly measure solute concentrations in the matrix phase with experimental uncertainties determined solely by atom-counting statistics [22–24]. Electrical resistivity is frequently used to measure supersaturation, and has been used for Al–Sc alloys [25–27]. This method is indirect, however, as it requires the use of external standards to determine the specific resistivity of Sc, Er or Yb in α-Al. Other analytical methods that measure concentrations directly often sample volumes that are too large and are thus influenced by precipitates, and do not determine a true matrix composition or are limited to surfaces whose compositions may be affected by oxide

* Corresponding author. Present address: Momentive Performance Materials, 24400 Highland Rd., Richmond Heights, OH 44124, USA.
E-mail address: vandalen@u.northwestern.edu (M.E. van Dalen).
[1] Present address: Sandia National Laboratories, MS-9404, 7011 East Ave., Livermore, CA 94550, USA.

1359-6454/$36.00
doi:10.1016/j.actamat.2009.05.007

layers. APT is therefore unique in being a bulk analysis technique that permits chemical analyses of the matrix phase and nanoscale precipitates independent of one another.

We describe herein the microstructural evolution caused by thermal aging of binary α-Al alloys with 0.03–0.06 at.% Er or Yb, which were chosen partly because of their lower cost as compared to Tm and Lu. Hereafter, all concentrations are given in atomic percent (at.%) unless otherwise noted. The temporal evolution of the mean Al_3RE precipitate radius, $\langle R(t)\rangle$, and the α-Al matrix supersaturation of REs, $\Delta C^{\alpha}_{RE}(t)$, were measured at 300 °C. The RE diffusivities in α-Al and the α-Al/Al_3RE interfacial free energies were calculated from the coarsening kinetics (Ostwald ripening) using a modified Lifshitz–Slyozov–Wagner (LSW) model for a dilute binary alloy; these physical quantities were heretofore unknown and are important for understanding Al–Sc–RE alloys. Also, measurements of the RE solid-solubility in α-Al near the eutectic temperatures and at 300 °C were determined, thereby providing information on the solvus curve, which had heretofore been unknown [6–8].

2. Experimental procedures

Three Er-containing alloys (Al–0.03Er, Al–0.045Er and Al–0.06Er) and two Yb-containing alloys (Al–0.03Yb and Al–0.06Yb) were cast and their exact compositions, as verified using direct-coupled plasma mass spectroscopy (ATI Wah Chang: Albany, OR), are given in Table 1. One Sc-containing alloy (denoted Al–0.12Sc) served as a control [28]. First, Al–RE master alloys were processed by arc-melting 99.9% pure Er or Yb (Stanford Materials) with 99.999% pure Al (the largest impurity being 1 at. ppm Si, as verified by glow-discharge mass spectrometry by the Evans Analytical Group: Syracuse, NY). Dilution casting to the final alloy compositions was performed in air, with the same 99.999% pure Al and the Al–RE master alloys, in a copper wedge with a 7° angle to ensure relatively fast cooling and solidification, with the exceptions of Al–0.03RE and Al–0.12Sc, which were cast into a graphite mold. The cast alloys were homogenized in a furnace with ±1 °C thermal stability for 72 h. The Al–Er and Al–Sc alloys were homogenized at 640 °C and the Al–Yb alloys were homogenized at 625 °C [6,7] so as not to exceed their respective eutectic temperatures. Homogenization was terminated by a water quench to ambient room temperature and no evidence of melting was observed. The Al–RE and Al–Sc alloys were immediately aged isochronally in air using either (i) 25 °C increments for 1 h or (ii) 50 °C increments for 2 h. Subsequent isothermal aging was performed on samples that had undergone an isochronal aging treatment to 300 °C.

Table 1
Overall RE concentrations in alloys as measured by direct-coupled plasma-spectroscopy (DCP) and APT.

Alloy	RE concentration from DCP (at.%)	RE concentration from APT (at.%)
Al–0.03Er	0.031(1)	0.0292(5)
Al–0.045Er	0.044(1)	0.0453(7)
Al–0.06Er	0.059(1)	–[a]
Al–0.03Yb	0.027(1)	–[a]
Al–0.06Yb	0.060(1)	–[a]

The uncertainty is given in parentheses after the least significant digit to which it applies.
[a] Not measured because the solid-solubility in Al is exceeded.

Samples with a final aging temperature below 100 °C were mounted in epoxy with a peak curing temperature of 28 °C, while the other samples were mounted in acrylic with a 79 °C peak curing temperature. Vickers microhardness measurements were performed at room temperature using a 200 g load with a 5 s dwell time on aged samples mechanically polished to a 1 μm surface finish. Ten microhardness measurements were performed on each sample and reported errors are one standard deviation from the mean.

Sample blanks for atom-probe tomography were produced by mechanically grinding material to a square cross-section of ~300 × 300 μm^2. An atomically sharp tip was then created by electropolishing. Initial electropolishing was performed using an electrolytic solution of 10 vol.% perchloric acid in acetic acid and a final electropolishing was performed using an electrolytic solution of 2 vol.% perchloric acid in butoxyethanol. APT was performed using a 3-D LEAP Si tomograph (Imago Scientific Instruments, Madison, WI) [29,30] operating in the voltage-pulsing mode at a specimen temperature of 30 K, a pulse repetition rate of 200 kHz and a 20% pulse fraction (pulse voltage increment divided by stationary-state DC voltage).

Transmission electron microscopy (TEM) was performed on Al–0.045Er and Al–0.03Yb using a Hitachi 8100 operating at an accelerating voltage of 200 kV. Thin foils were mechanically ground to a thickness of 200 μm and subsequently electropolished in an electrolytic solution of 5 vol.% perchloric acid in methanol at −30 to −40 °C, which was cooled using a bath of dry ice in methanol. The precipitate radii, R, as measured by TEM, were checked for consistency using APT but, because of the small precipitate volume fractions and the small APT analysis volumes (ca. 50 × 50 × 500 nm^3), the TEM results of $\langle R(t)\rangle$ were used for precipitate coarsening calculations.

3. Results

3.1. Maximum RE solid-solubility

In the two homogenized and as-quenched Al–0.06RE alloys, micron-sized eutectic precipitates are visible in scanning electron microscopy micrographs, indicating that the

RE solid-solubility had been exceeded. The RE solubilities in the α-Al matrix of the two Al–0.06RE alloys after homogenization and quenching (assuming that additional solute had not precipitated during the quenching procedure) were determined by APT measurements to be 0.0461 ± 0.006 at.% for Er at 640 °C and 0.0248 ± 0.007 at.% for Yb at 625 °C.

These experimentally measured maximum solubilities were used to select the compositions of the more dilute Al–RE alloys for subsequent microstructural temporal evolution studies, such that the maximum volume fraction of Al_3RE precipitates could be obtained upon aging, with most of the solute remaining in the α-Al matrix after homogenization and quenching. The volume fraction, ϕ, of precipitates in these more dilute alloys at 300 °C was small: $\phi = 0.14 \pm 0.03\%$ for Al–0.045Er and $\phi = 0.11 \pm 0.02\%$ for Al–0.03Yb, as determined by comparing the APT measurements of the RE solute concentrations after homogenization with the concentration of solute remaining in solution in the α-Al matrix after aging, assuming that the solute not in the α-Al matrix forms precipitates with the stoichiometric trialuminide compositions, Al_3Er or Al_3Yb.

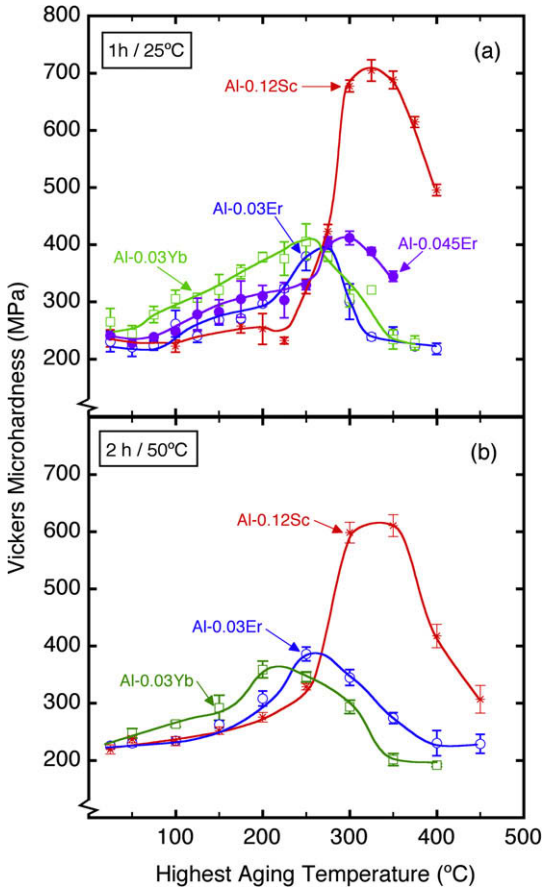

Fig. 1. Vickers microhardness vs. highest aging temperature for Al–0.03Er, Al–0.045Er, Al–0.03Yb and Al–0.12Sc isochronally aged: (a) for 1 h time intervals with 25 °C temperature intervals; (b) for 2 h time intervals with 50 °C temperature intervals.

3.2. Microhardness and homogeneous or heterogeneous Al_3RE precipitation

The Vickers microhardness was measured after each step in the isochronal aging experiments performed on the more dilute Al–RE alloys (Fig. 1). The motivation for isochronally aging from low-to-high temperatures is to promote homogeneous nucleation of Al_3RE precipitates at the lowest temperatures possible, or at least a homogeneous distribution of precipitates. With increasing aging temperature, the RE supersaturation in the α-Al matrix decreases and hence the chemical driving force for precipitation decreases continuously. Aging at lower temperatures may promote homogeneous nucleation, as the net reversible work to make a critical size nucleus for homogeneous nucleation decreases with decreasing temperature, i.e. increasing supersaturation. Furthermore, at higher temperatures heterogeneous nucleation dominates since the nucleation current for heterogeneous nucleation on dislocations or other lattice imperfections is larger than for homogeneous nucleation [31,32].

The onset of age hardening for Al–0.03Er occurs at 150 °C and for Al–0.03Yb it begins below 100 °C (Fig. 1a). The microhardness value peaks at 275 °C for Al–0.03Er and 250 °C for Al–0.03Yb, despite the somewhat greater precipitate volume fraction present in the Al–Er alloy. A decrease in microhardness is observed for both alloys at higher temperatures, which is indicative of precipitate coarsening (Ostwald ripening). Also shown in Fig. 1a is the hardening behavior of Al–0.045Er, which is close to that of Al–0.03Er, except for a higher maximum hardness and peak-aging temperature, as anticipated from the higher supersaturation in Al–0.045Er. Despite the much higher supersaturation of Sc in Al–0.12Sc, this alloy shows no significant increase in microhardness until 250 °C, but, as anticipated, it exhibits a larger peak hardness value. The slower precipitation kinetics of Al–0.12Sc are because Sc's activation energy for diffusion in Al is greater than that of Er or Yb (see Section 4.3). Isochronal aging with larger temperature and time steps results in essentially the same hardness evolution (Fig. 1b).

Fig. 2a displays a TEM micrograph of an Al–0.03Yb specimen aged isochronally to 300 °C in 25 °C/1 h time intervals. Some Al_3Yb precipitates have heterogeneously nucleated along dislocations, which are surrounded by precipitate-free zones. These precipitates have a mean radius, $\langle R \rangle \approx 10$ nm, which is larger than those that are homogeneously distributed, $\langle R \rangle = 3.8 \pm 0.8$ nm, the latter being coherent with the α-Al matrix, as determined by the observable Ashby–Brown strain-field contrast in TEM micrographs (not displayed). Fig. 2b shows a TEM micrograph of a region of homogeneously distributed Al_3Er precipitates, $\langle R \rangle = 17 \pm 6$ nm, which formed in Al–0.045Er after isochronal aging to 300 °C, with 25 °C/1 h time intervals, followed by isothermal aging for 1536 h (64 days) at 300 °C. Despite their large radii, the Al_3Er precipitates in

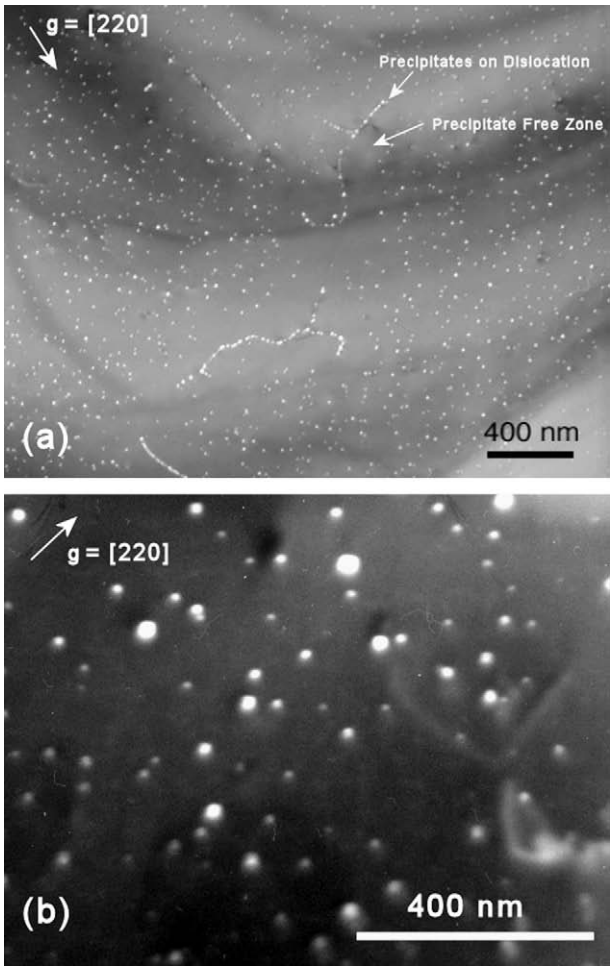

Fig. 2. Superlattice dark-field two-beam TEM micrographs for alloys aged isochronally to 300 °C in 25 °C increments for 1 h time intervals for: (a) Al–0.03Yb with no additional aging, exhibiting coherent Al_3Yb precipitates ([1 1 1] projection), and (b) for Al–0.045Er alloy with additional aging at 300 °C for 64 days, displaying coherent Al_3Er precipitates ([0 0 1] projection).

these regions remain coherent with the α-Al matrix, as determined from strain-field contrast in TEM micrographs.

3.3. Temporal evolution of mean precipitate radius and α-Al matrix supersaturation during aging at 300 °C

The temporal evolution of the mean Al_3RE precipitate radius, $\langle R(t)\rangle$, and the RE matrix supersaturations, $\Delta C^{\alpha}_{RE}(t)$, were measured after aging at 300 °C using TEM and APT, respectively, for Al–0.045Er and Al–0.03Yb specimens, which had been first subjected to a 25 °C/1 h time interval isochronal aging treatment to 300 °C. Figs. 3 and 4 demonstrate that $\langle R(t)\rangle$ is increasing and $\Delta C^{\alpha}_{RE}(t)$ is concomitantly decreasing with increasing aging time at constant temperature. Data for precipitate radii were gathered in multiple regions of specimens with homogeneous spatial distributions of precipitates at least 100 nm from any precipitates heterogeneously nucleated on dislocations. The areas away from the dislocations are chosen because

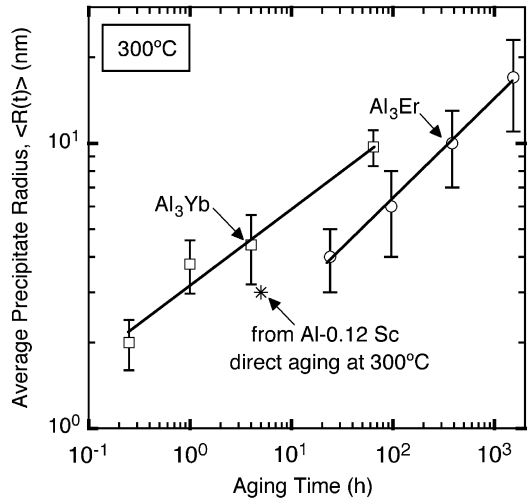

Fig. 3. Average precipitate radius, $\langle R(t)\rangle$, for Al–0.045Er and Al–0.03Yb alloys as a function of isothermal aging time at 300 °C, after isochronal aging to 300 °C in 25 °C temperature increments for 1 h time intervals.

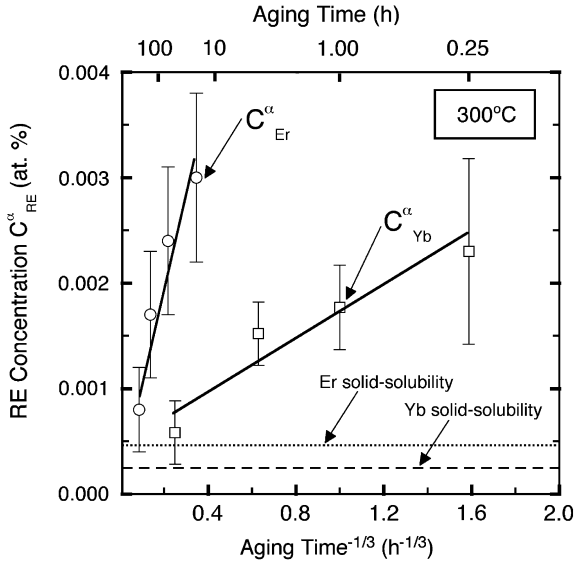

Fig. 4. Concentration of Er and Yb in the α-Al matrix as a function of isothermal aging time raised to the −1/3 power for Al–0.045Er and Al–0.03Yb alloys after isochronal aging to 300 °C in 25 °C increments for 1 h time intervals. The solid-solubilities are obtained by extrapolating to infinite time on the abscissa.

the effect of dislocations on solute diffusion diminishes with increasing distance from a dislocation.

According to the classical LSW model for precipitate coarsening in a dilute binary alloy [33–35], the quantity $\langle R(t)\rangle$ at a time t is given by:

$$\langle R(t)\rangle^n - \langle R(t_0)\rangle^n = K(t - t_0) \quad (1)$$

where $R(t_0)$ is the radius at time t_0, n is a temporal exponent, and K is a rate constant: t_0 is the time that quasi-stationary-state coarsening commences, which is the time when the equilibrium volume fraction is close to being achieved. The LSW value for n is 3. A double regression

Table 2
The time exponents and coarsening constants for Al–0.03Yb and Al–0.045Er alloys determined experimentally employing APT measurements.*

Alloy	$1/n$ (Eq. (1))	m (Eq. (4))	K, (Eq. (1)) (m3 s^{-1})	κ (Eq. (4)) (s^{-1})
Al–0.045Er	0.36 ± 0.03	-0.30 ± 0.09	$(2 \pm 1) \times 10^{-31}$	$(1.1 \pm 0.9) \times 10^{7}$
Al–0.03Yb	0.26 ± 0.02	-0.27 ± 0.02	$(3.9 \pm 0.1) \times 10^{-30}$	$(7.0 \pm 0.8) \times 10^{10}$

* See Section 3.3 for definitions of $1/n$, m, K, and κ.

analysis of the data in Fig. 3 results in values for K and n (Table 2). The temporal exponent $1/n$ is 0.36 ± 0.03 for Al–Er and 0.26 ± 0.02 for Al–Yb. Thus, the Al–Er alloy is close to the LSW value of 1/3, while the Al–Yb alloy has a somewhat lower value.

The rate constant K in the Calderon et al. modified LSW model for a binary alloy is given by [36]:

$$K = \frac{4Dl^{\alpha}}{9(C_e^{\beta} - C_e^{\alpha})} \tag{2}$$

where D is the diffusivity of the solute, l^{α} is the capillary length, and C_e^{β} and C_e^{α} are the equilibrium RE concentrations in the matrix (α) and precipitate (β) phases, respectively. The equation for l^{α} is given by [36]:

$$l^{\alpha} = \frac{2V_m^{\beta}\gamma^{\mathrm{Al/Al_3RE}}}{G_m^{\alpha''}(C_e^{\beta} - C_e^{\alpha})} \tag{3}$$

where V_m^{β} is the molar volume of the precipitate phase, Al_3RE, $\gamma^{\mathrm{Al/Al_3RE}}$ is the interfacial free energy between the α-Al matrix and Al_3RE precipitates, and $G_m^{\alpha''}$ is the second derivative of the molar free energy of the α-Al matrix with respect to composition evaluated at C_e^{α}.

Furthermore, the modified LSW model predicts that the supersaturation of a RE element in the α-Al matrix is given by:

$$\Delta C_{\mathrm{RE}}^{\alpha}(t) = (\kappa(t - t_o))^{-m} \tag{4}$$

where m is the temporal exponent and κ is a rate constant; the LSW value of m is 1/3. The α-Al matrix supersaturation, $\Delta C_{\mathrm{RE}}^{\alpha}(t)$, is given by $C_{\mathrm{RE}}^{\alpha}(t) - C_{\mathrm{RE}}^{\alpha}(t_{\infty})$, where $C_{\mathrm{RE}}^{\alpha}(t)$ is the concentration of a RE in the α-Al matrix at time t and $C_{\mathrm{RE}}^{\alpha}(t_{\infty})$ is the concentration of a RE in the matrix at infinite time. The value of $\Delta C_{\mathrm{RE}}^{\alpha}(t)$ is obtained as follows. First, the measured Yb and Er concentrations, $C_{\mathrm{RE}}^{\alpha}(t)$, are plotted vs. $(t)^{-1/3}$ and a linear extrapolation to infinite time is made to obtain the solid-solubilities of Er or Yb in α-Al at 300 °C (Fig. 4). This extrapolation yields $C_{\mathrm{Er}}^{\alpha}(t_{\infty}) = (4 \pm 3) \times 10^{-4}$ at.% Er and $C_{\mathrm{Yb}}^{\alpha}(t_{\infty}) = (2.9 \pm 0.5) \times 10^{-4}$ at.% Yb (Table 2). Secondly, the RE α-Al matrix supersaturation, $\Delta C_{\mathrm{RE}}^{\alpha}(t)$, is then obtained by subtracting the value of $C_{\mathrm{RE}}^{\alpha}(t_{\infty})$ from $C_{\mathrm{RE}}^{\alpha}(t)$. It is strongly emphasized that $C_{\mathrm{RE}}^{\alpha}(t)$ is measured by APT in regions where the precipitates are homogeneously distributed and *not* where they are heterogeneously distributed. Fig. 5 displays a plot of $\Delta C_{\mathrm{RE}}^{\alpha}(t)$ vs. time and the exponent m is found to be 0.30 ± 0.09 for Al–Er and 0.27 ± 0.02 for Al–Yb utilizing a double regression analysis. Values for κ from this fit are reported in Table 2. The rate constant κ is given by the modified LSW model for a binary alloy:

$$\kappa = \frac{9(l^{\alpha})^2(C_e^{\beta} - C_e^{\alpha})}{4D} \tag{5}$$

The third prediction of the LSW model concerns the temporal evolution of the number density of precipitates, N_v, which is proportional to the temporal power -1. It is not discussed herein because we do not require it for determining either the solid-solubilities or the diffusivities.

4. Discussion

4.1. Maximum RE solubility in Al

The near-eutectic solid-solubility of Er in Al (0.0461 ± 0.006 at.% at 640 °C) is about twice that of Yb in Al (0.0248 ± 0.007 at.% at 625 °C), which are both at least four to five times smaller than that of Sc in Al (0.23 at.% at the eutectic temperature of 660 °C and 0.18 at.% at 640 °C) [25,37,38]. Thus, smaller volume fractions of Al_3RE precipitates ($\phi = 0.11$–0.14%) are obtained for the Al–Er and Al–Yb alloys upon cooling from a near-eutectic homogenization temperature, as compared to the Al_3Sc volume fraction attainable for binary Al–Sc alloys; $\phi = 0.95\%$ at 300 °C, as determined by use of the lever rule and an extrapolation of the Al–Sc solvus line [38]. The significantly smaller solid-solubilities of Er and Yb in α-Al as compared to Sc imply that the Al–Er and Al–Yb systems are less promising than the Al–Sc system for designing high-strength high-temperature alloys that are resistant to

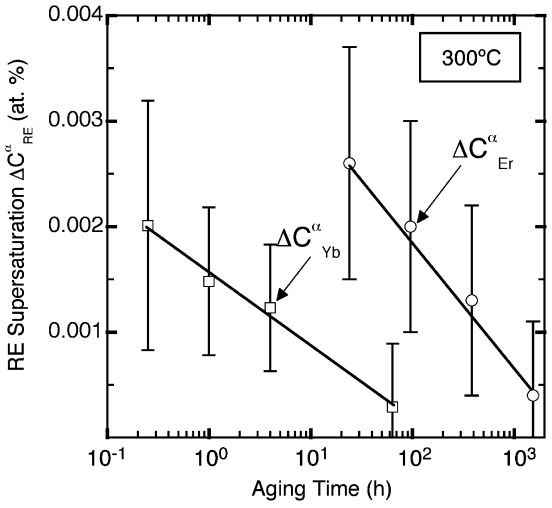

Fig. 5. The α-Al matrix RE supersaturations for Al–0.045Er and Al–0.03Yb alloys as a function of isothermal aging time at 300 °C after isochronal aging to 300 °C in 25 °C increments for 1 h time intervals.

coarsening. However, small Er or Yb additions to Al–Sc alloys result in ternary alloys with hardness and aging behavior that are similar to those of binary Al–Sc alloys [1], as well as similar enhanced creep resistance [10,11]. Furthermore, these ternary alloys are less expensive than binary Al–Sc alloys because Sc is more expensive than the RE elements.

4.2. Al_3RE precipitation kinetics

Precipitation occurs at lower temperatures in the Al–Yb alloy than in the Al–Er and Al–Sc alloys, as demonstrated by isochronal aging experiments employing either 25 °C or 50 °C increments (Fig. 1). These results suggest that Yb diffuses faster than Er and Sc in the α-Al-matrix at these lower temperatures. An interesting feature of Fig. 1 is that the microhardness of Al–Yb is greater at 25 °C than in the range 350–400 °C after extensive coarsening of the precipitates. This indicates that the Al–Yb alloy most likely undergoes some clustering or precipitation during quenching from the homogenization temperature to ambient room temperature or upon subsequent holding at ambient room temperature prior to the microhardness measurements, most likely due to quenched-in lattice vacancies. Since Er atoms begin to cluster or precipitate at temperatures between those for Yb and Sc, it is anticipated that the diffusivity of Er in α-Al is intermediate between those of Yb and Sc: see Section 4.3. Finally, the Al–0.045Er alloy exhibits a peak microhardness value that is ~25 MPa greater than the value for the Al–0.03Er alloy (Fig. 1a). Though this difference is close to the experimental error, it is expected based on the larger precipitate volume fraction in the more concentrated Al–0.045Er alloy.

The process of aging specimens initially at low temperatures and increasing the temperature isochronally did not succeed in creating a fully homogeneous distribution of Al_3RE precipitates at 300 °C (Fig. 2). This temperature is, however, above the peak hardness temperature and it is possible that underaged specimens exhibit more uniform precipitate distributions. The heterogeneous distribution of precipitates at 300 °C in the Al–RE alloys is caused by the small driving force for precipitation caused by the low solute concentrations, which are, of course, dictated by the small RE solubilities in α-Al. At lower temperatures, however, a homogeneous distribution of precipitates may be more favorable due to the smaller diffusivities and higher supersaturations. In contrast to the Al–RE alloys, binary Al–Sc alloys containing solute concentrations below the maximum solid-solubility of 0.23 at.% [25,28,39–42] exhibit homogeneous distributions of coherent Al_3Sc precipitates upon direct isothermal aging at 300 °C. The value of $\langle R(t)\rangle$ is consistently smaller in the Al–0.12Sc alloy (Fig. 3), even though this alloy was isothermally aged directly at 300 °C. The reason for this result is the higher nucleation current due to the smaller net reversible work to make a nucleus in Al–0.12Sc. Additionally, an Al–0.06Sc–0.06Ti alloy aged at 300 °C exhibited homogeneously distributed Al_3(Sc, Ti) precipitates, whereas at 330 °C extensive heterogeneous nucleation on dislocations was observed [43]. The latter behavior is explained by the concomitant decreasing chemical driving force for precipitation with increasing aging temperature and the small diffusivity of Ti in Al.

Fig. 1a indicates that the microhardness of Al–0.03Yb increases at temperatures up to ~250 °C, which shows that Al_3Yb precipitation is occurring over a wide range of temperatures. For Al–0.045Er, Al_3Er precipitation commences at 150 °C, with increasing microhardness values up to 300 °C. Upon subsequent isothermal aging at 300 °C, Al–0.045Er and Al–0.03Yb both exhibit precipitate coarsening, with $\langle R(t)\rangle$ proportional to $t^{1/n}$ (Fig. 3), where $1/n$ is 0.36 ± 0.09 for Al–0.045Er and 0.26 ± 0.02 for Al–0.03Yb. Thus, the Al–Er alloy is closer to the 1/3 value predicted by the LSW model and Al–Yb has a $1/n$ value close to 1/4.

The LSW model, which is a mean-field model, is based on many strong physical assumptions, which include: (i) a negligible volume fraction of precipitates; (ii) an ideal binary solid-solution; (iii) a stationary-state evolution; (iv) no elastic interactions among precipitates; (v) no overlap of the diffusion fields of individual precipitates; (vi) an equilibrium value for the composition of the precipitate phase, which is considered to be essentially pure solute; and (vii) coarsening is diffusion-limited and occurs by the evaporation–condensation mechanism. Hence, it is not surprising that we do not obtain exact agreement with the temporal exponent value of 1/3 for $\langle R(t)\rangle$ for the Al–RE alloys. To obtain an accurate value of $1/n$ one needs ideally to have an $\langle R(t)\rangle$ value that increases by a factor of ca. 10 from its initial value during the quasi-stationary-state coarsening regime, which is not the case for either Al–Er or Al–Yb. Also for $1/n$ to be equal to 1/3 for diffusion-limited coarsening, $\langle R(t_0)\rangle$ must be significantly less than $\langle R(t)\rangle$.

4.3. RE diffusivities in α-Al

The RE diffusivities in α-Al at 300 °C, D_{RE}, are calculated using the same approach as in Ref. [44], which examined different Ni-based binary alloys and assumed ideal solution theory. By using the relationship between κ and K, Eqs. (2) and (5), it is possible to eliminate the interfacial energy, γ^{Al/Al_3RE}, and the capillary length to obtain:

$$D_{RE} = \frac{9(C_e^{\beta} - C_e^{\alpha})}{4}\left(K^2\kappa\right)^{1/3} \tag{6}$$

The coarsening rate constants K and κ (Table 2) are determined experimentally from the temporal evolution of $\langle R(t)\rangle$ and $\Delta C_{RE}^{\alpha}(t)$ at 300 °C (Figs. 3 and 4).

The diffusivities of Er and Yb in Al at 300 °C calculated from Eq. (6) are $D_{Er} = (4 \pm 2) \times 10^{-19}$ and $D_{Yb} = (6 \pm 2) \times 10^{-17}$ m^2 s^{-1}, respectively, with the experimental errors being propagated from each parameter in Eq. (6). The present method, which relies on precipitate coarsening data to determine the diffusivity of solutes in very dilute binary alloys at low temperatures, has greater accuracy

than alternative techniques, e.g. radioactive tracer methods, which have poorer spatial resolution.

Despite differences between the two Al–RE alloys in their solid-solubilities, these diffusivity results are consistent with the hardness evolution results displayed in Fig. 1a, which indicates that the activation energy for solute diffusion in α-Al decreases from Yb to Er to Sc, based on the temperatures observed for the first hardness increases and peak hardness values. (This observation is qualitative, since microhardness is affected by several physical quantities.) As illustrated in Fig. 6, the value for D_{Yb} in Al is large compared to D_{Er}, as reported herein, and to five lighter lanthanides (La, Ce, Pr, Nd and Sm), which were extrapolated to 300 °C from data obtained above 450 °C [45–47]. In fact, D_{Yb} is larger than the tracer diffusivity of Al in Al at 300 °C ($D_{Al}(300\,°C) = 2.63 \times 10^{-17}\,m^2\,s^{-1}$ [48]) by a factor of 3.04 to 1.52. $D_{Yb}(300\,°C)$ is similar to the diffusivities of Ni and Cu in Al at 300 °C (2.2×10^{-17} and $2.6 \times 10^{-17}\,m^2\,s^{-1}$, respectively [49]).

The approximate similarity of the Er diffusivity value with those of the other lanthanides and the large diffusivity of Yb in α-Al are somewhat consistent with the physical properties of the lanthanides. Ytterbium has a lower melting temperature (824 °C) than Er (1497 °C) and the other lanthanides, which increase from 920 to 1545 °C with increasing atomic number, Z, with the exceptions of Ce (795 °C), Eu (826 °C) and Yb. Also, Yb is the only RE with a face-centered cubic crystal structure; all the other REs have a hexagonal close-packed structure except for the body-centered cubic Eu and the trigonal Sm. Finally, Yb has an anomalous valence state in Al compared with the other lanthanides (again except Eu) and has much different enthalpies of formation for the Al_2RE and Al_3RE phases

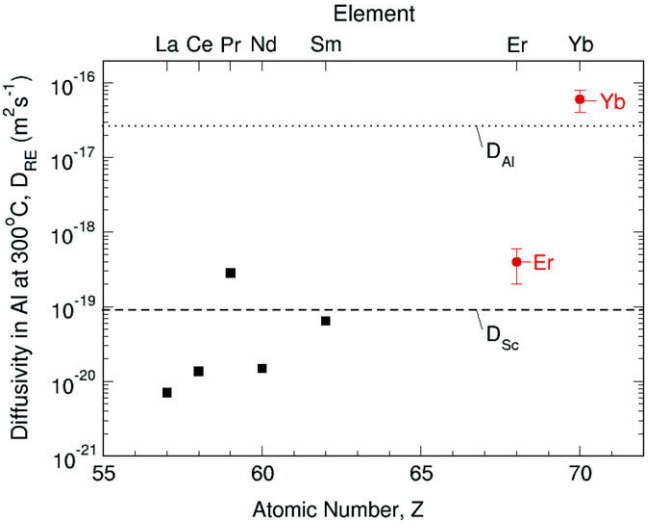

Fig. 6. Experimentally determined diffusivities of Er and Yb in Al at 300 °C via 3-D APT, compared to literature values for the diffusivities of Sc [45] and light lanthanides in Al, which were extrapolated to 300 °C from data taken above 450 °C [45–47] and the Al tracer diffusivity in Al at 300 °C [46], which is indicated by the dashed horizontal line. The tracer diffusivity of Sc in Al is also indicated by a dashed horizontal line.

[50,51]. To understand all the observations regarding RE diffusion in Al requires first-principles calculations using local-density functional theory, which is beyond the scope of this article.

Since the diffusivities of Er and Yb in Al are greater than that of Sc in Al at 300 °C [45], additions of Er or Yb should not retard the coarsening kinetics of ternary Al–Sc–Er or Al–Sc–Yb alloys compared to binary Al–Sc alloys with the same solute concentration, which is in agreement with experimental measurements [1,10]. This is unlike the strong retarding effect of slowly diffusing Ti or Zr atoms on the coarsening kinetics of Al–Sc alloys [43,52–54]. Scandium additions to Al–Er or Al–Yb alloys may, however, slow the coarsening kinetics of Al_3(RE, Sc) precipitates. This is analogous to the reduction of the coarsening kinetics observed in ternary Al–Li–Sc alloys as compared to Al–Li alloys [55], with Li diffusing significantly faster than Sc in Al [46]. The addition of Sc to Al–Li alloys also leads to a higher number density of smaller Al_3Li ($L1_2$) precipitates with a core–shell structure [55–57], a situation that also occurs in Al–Sc–RE alloys [1,58].

4.4. Al/Al_3RE interfacial free energy

The α-Al/Al_3RE interfacial free energy, γ^{Al/Al_3RE}, is calculated using an expression for the rate constant K in Eq. (2) valid for an ideal binary alloy developed by Calderon et al. [36]:

$$\gamma^{Al/Al_3RE} = \frac{9R_gT(C_e^{\beta} - C_e^{\alpha})^2}{8D_{RE}V_m^{\beta}C_e^{\alpha}(1 - C_e^{\alpha})}K \tag{7}$$

where R_g is the ideal gas constant, V_m^{β} is the molar volume of the precipitate phase ($1.12 \times 10^{-5}\,m^3\,mol^{-1}$ for Al_3Yb and $1.13 \times 10^{-5}\,m^3\,mol^{-1}$ Al_3Er as calculated from the Al_3RE lattice parameters) and D_{RE} is the diffusion coefficient of the RE in α-Al. Eq. (7) yields values of $\gamma^{Al/Al_3Er} = 0.4 \pm 0.2\,J\,m^{-2}$ and $\gamma^{Al/Al_3Yb} = 0.6 \pm 0.3\,J\,m^{-2}$ at 300 °C, which are based on the assumption of an ideal solution. These values are larger than those found in the Al–Sc system, with $\gamma^{Al/Al_3Sc} \approx 0.2\,J\,m^{-2}$ [28,59]. The values of the interfacial energies for the Al–RE alloys are associated with uncertainties that are quite high: ~50% of the measured values. Although the Al–Sc value is just at the minimum of the uncertainty range, these high values of γ^{Al/Al_3RE} may explain why precipitates in the Al–RE alloys have a tendency to nucleate more heterogeneously than in the Al–Sc alloys at temperatures greater than 300 °C. That is, the larger values of γ^{Al/Al_3RE} imply a larger value of the net reversible work to make a critical size nucleus and a larger critical nucleus radius, and concomitantly a smaller homogeneous nucleation current.

5. Conclusions

Upon aging at elevated temperatures, binary aluminum alloys containing 0.03–0.06 at.% Er or Yb form nanosize

Al_3Er or Al_3Yb precipitates with the $L1_2$ structure. This precipitation process is studied using Vickers microhardness, TEM and 3-D APT. The following are the key results of our study of these Al–Er and Al–Yb alloys:

- The maximum RE solid-solubilities in α−Al, as measured by 3-D APT, are 0.0461 ± 0.0006 at.% Er and 0.0248 ± 0.0007 at.% Yb at 640 and at 625 °C, respectively. Both values are smaller than the maximum solubility of Sc in Al (0.23 at.%). Hence, the maximum volume fraction of Al_3Yb ($\phi = 0.11\%$) or Al_3Er ($\phi = 0.14\%$) precipitates is smaller than that of Al_3Sc ($\phi = 0.95\%$) in binary alloys.
- Measurements of microhardness utilizing isochronal aging experiments demonstrate that Er precipitation is initiated at 150 °C and an aging peak occurs at 275 °C for Al–0.03Er, while for Al–0.03Yb precipitation of Yb is initiated at 100 °C and an aging peak occurs at 250 °C. These temperatures are significantly lower than for a control Al–0.12Sc alloy, which is because the diffusivities of Er and Yb are greater than that of Sc in Al.
- The coarsening rate temporal exponent, $1/n$, for the mean radius, $\langle R(t)\rangle$, at 300 °C of the Al_3Er and Al_3Yb precipitates in Al–0.045Er and Al–0.03Yb alloys is 0.36 ± 0.03 and 0.26 ± 0.02, respectively. Hence, the Al–Er alloy has a $1/n$ that is close to the 1/3 value of the LSW model for an ideal solution, while the $1/n$ value of the Al–Yb is close to 1/4.
- The coarsening rate temporal exponent, m, for the matrix supersaturation, $\Delta C^{\alpha}_{RE}(t)$, at 300 °C of the Al_3Er and Al_3Yb precipitates in Al–0.045Er and Al–0.03Yb alloys is -0.30 ± 0.09 and -0.27 ± 0.02, respectively. Therefore, the Al–Er alloy has an m value that is close to the $-1/3$ value of the LSW model, while the Al–Yb alloy has a value close to $-1/4$.
- The diffusivity in Al at 300 °C is determined from the isothermal evolution of $\langle R(t)\rangle$ and $\Delta C^{\alpha}_{RE}(t)$, yielding values of $(4 \pm 2) \times 10^{-19}\ m^2\ s^{-1}$ for Er and $(6 \pm 2) \times 10^{-17}\ m^2\ s^{-1}$ for Yb. Both elements diffuse significantly faster than does Sc in Al ($9 \times 10^{-20}\ m^2\ s^{-1}$).
- The Al/Al_3RE interfacial free energies, γ^{Al/Al_3RE}, calculated from the isothermal coarsening data at 300 °C, are $\gamma^{Al/Al_3Er} = 0.4 \pm 0.2$ and $\gamma^{Al/Al_3Yb} = 0.6 \pm 0.3\ J\ m^{-2}$, both of which are greater than $\gamma^{Al/Al_3Sc} \approx 0.2\ J\ m^{-2}$ [28,59].
- Achieving a high number density of coarsening-resistant precipitates that are homogeneously distributed is easier for Al–Sc alloys than for the two Al–RE alloys studied because of: (i) the tendency for Al_3RE precipitates to nucleate heterogeneously because of the small chemical driving force for precipitation; (ii) the higher Al_3RE coarsening rates due to the higher RE diffusivities and larger α-Al/Al_3RE interfacial energies; and (iii) the smaller Al_3RE volume fractions due to the smaller RE maximum solubilities in Al.

Acknowledgements

This research was supported by the US Department of Energy through grant DE-FG02-98ER45721. APT measurements were performed at the Northwestern University Center for Atom-Probe Tomography (NUCAPT) using a 3-D local-electrode atom-probe tomograph purchased with funding from the NSF-MRI (DMR-0420532, Dr. Charles Bouldin, monitor) and ONR-DURIP (N00014-0400798, Dr. Julie Christodoulou, monitor) programs. Research Assistant Prof. Dieter Isheim (NUCAPT) is kindly thanked for useful discussions and for managing NUCAPT. Susan Farjami and Peter Voorhees are thanked for interesting discussions and calculation of screening distances.

References

[1] Karnesky RA, Van Dalen ME, Dunand DC, Seidman DN. Scripta Mater 2006;55:437.
[2] Zalutskaya OI, Ryabov VG, Zalutskii II. Dop Akad Nauk Ukrain, RSR 1969:255.
[3] Palenzona AJ. J Less-Common Metals 1972;29:289.
[4] Harada Y, Dunand DC. Mater Sci Forum 2007;539–543:1565.
[5] Harada Y, Dunand DC. Intermetallics 2009;17:17.
[6] Kononenko VI, Golubev SV. Russian Metall 1990;2:197.
[7] Massalski. Binary alloy phase diagrams. ASM Int.; 1990.
[8] Meng FG, Zhang LG, Liu HS, Liu LB, Jin ZP. J Alloys Compds 2008;452:279.
[9] Zalutskaya OI, Kontseyoy VG, Karamishev NI, Ryabov VR, Zalutskii II. Dop Akad Nauk Ukrain. RSR 1970:751.
[10] Van Dalen ME, Dunand DC, Seidman DN. J Mater Sci 2006;41:7814.
[11] Karnesky RA, Seidman DN, Dunand DC. Mater Sci Forum 2006;519–521:1035.
[12] Marquis EA, Dunand DC. Scripta Mater 2002;47:503.
[13] Nie Z, Jin T, Fu J, Xu G, Yang J, Zhou J, et al. Mater Sci Forum 2002;396–402:1731.
[14] Nie Z, Jin T, Zou J, Fu J, Yang J, Zuo T. Trans Nonferrous Metals Soc China 2003;13:509.
[15] Nie ZR, Fu JB, Zou JX, Jin TN, Yang JJ, Xu GF, et al. Mater Sci Forum 2004:28.
[16] Fu J, Nie Z, Jin T, Zou J, Zuo T. J Rare Earths 2005;23:430.
[17] Xu G, Mou S, Yang J, Jin T, Nie Z, Yin Z. Trans Nonferrous Metals Soc China 2006;16:598.
[18] Yang J, Nie Z, Jin T, Xu G, Fu J, Ruan H, et al. Trans Nonferrous Metals Soc China 2003;13:1035.
[19] Fang H, Chen K, Zhang Z, Zhu C. Trans Nonferrous Metals Soc China 2008;18:28.
[20] Zhang Z, Chen K, Fang H, Qi X, Liu G. Trans Nonferrous Metals Soc China 2008;18:1037.
[21] Song M, Wu Z, He Y. Mater Sci Eng A 2008;497:519.
[22] Kelly TF, Miller MK. Rev Sci Instr 2007;78:031101.
[23] Hellman OC, Vandenbroucke J, Blatz du Rivage J, Seidman DN. Mater Sci Eng A 2002;327:29.
[24] Hellman OC, Vandenbroucke JA, Rüsing J, Isheim D, Seidman DN. Micros Microanal 2000;6:437.
[25] Jo HH, Fujikawa SI. Mater Sci Eng A 1993;171:151.
[26] Royset J, Ryum N. Mater Sci Eng A 2005;396:409.
[27] Sano N, Hasegawa K, Jo H, Hirano K, Pickering H, Sakurai T. J Phys 1987;C6:337.
[28] Marquis EA, Seidman DN. Acta Mater 2001;49:1909.
[29] Seidman DN. Ann Rev Mater Res 2007;37:127.
[30] Kelly TF, Gribb TT, Olson JD, Martens RL, Shepard JD, Weiner SA, et al. Micros Microanal 2004;10:373.
[31] Cahn JW. Acta Metall 1956;6:572.

[32] Cahn JW. Acta Metall 1957;5:169.
[33] Ardell AJ. Precipitate coarsening in solids: modern theories, chronic disagreement with experiment. In: Lorimer GW, editor. Phase transformations '87. London: The Institute of Metals; 1988. p. 85.
[34] Lifshitz IM, Slyozov VV. J Phys Chem Solids 1961;19:35.
[35] Wagner CZ. Elektrochemistry 1961;65:581.
[36] Calderon HA, Voorhees PW, Murray JL, Kostorz G. Acta Metall Mater 1994;42:991.
[37] Okamoto H. Phase diagrams of dilute binary alloys. Materials Park (OH): ASM International; 2002.
[38] Murray JL. J Phase Equilib 1998;19:380.
[39] Tsivoulas D, Robson JD. Mater Sci Forum 2006;519-521:473.
[40] Royset J, Ryum N. Int Mater Rev 2005;50:1.
[41] Novotny GM, Ardell AJ. Mater Sci Eng A 2001;A318:144.
[42] Hyland RW. Metall Trans A 1992;23A:1947.
[43] Van Dalen ME, Dunand DC, Seidman DN. Acta Mater 2005;53:4225.
[44] Ardell AJ. Interf Sci 1995;3:119.
[45] Fujikawa SI. Defect Diffus Forum 1997;143–147:115.
[46] Mondolfo LF. Aluminum alloys: structure and properties. London: Butterworths; 1976.
[47] Murarka SP, Agarwala RP. Govt of India Atomic Energy Commun 1968.
[48] Peterson NL. J Nucl Mater 1978;69–70:3.
[49] Knipling KE, Dunand DC, Seidman DN. Z Metallk 2006;97:246.
[50] Borzone G, Cardinale AM, Parodi N, Cacciamani G. J Alloys Compd 1997:247.
[51] Pasturel A, Chatillon-Colinet C. J Less-Common Metals 1983;90:21.
[52] Clouet E, Lae L, Epicier T, Lefebvre W, Nastar M, Deschamps A. Nat Mater 2006;5:482.
[53] Lefebvre W, Danoix F, Da Costa G, De Geuser F, Hallem H, Deschamps A, et al. Surf Interf Anal 2007;39:206.
[54] Fuller CB, Seidman DN. Acta Mater 2005;53:5415.
[55] Joh CH, Yamada K, Miura Y. Mater Transact, JIM 1999;40:439.
[56] Krug ME, Dunand DC, Seidman DN. Appl Phys Lett 2008;92:124107.
[57] Radmilovic V, Miller MK, Mitllin D, Dahmen U. Scripta Mater 2006;54:1973.
[58] van Dalen ME. Ph.D. Thesis, Northwestern University; 2007.
[59] Asta M, Foiles SM, Quong AA. Phys Rev B 1998;57:11265.